Numerical study of the tide and tidal dynamics in the South China Sea

Tingting Zu[a], Jianping Gan[a,b,*], Svetlana Y. Erofeeva[c]

[a]*Atmospheric, Marine, Coastal Environment (AMCE) Program, Hong Kong University of Science and Technology, Clear Water Bay, Kowloon, Hong Kong*
[b]*Department of Mathematics, Hong Kong University of Science and Technology, Clear Water Bay, Kowloon, Hong Kong*
[c]*College of Oceanic and Atmospheric Sciences, Oregon State University, Corvallis, USA*

Abstract

Tides and their dynamic processes in the South China Sea (SCS) are studied by assimilating Topex/Poseidon altimetry data into a barotropic ocean tide model for the eight major constituents (M_2 S_2 K_1 O_1 N_2 K_2 P_1 Q_1) using a tidal data inversion scheme. High resolution ($\sim$10 km) and large model domain are adopted to better resolve the physical processes involved and to minimize the uncertainty from the open boundary condition. The model results, which are optimized by an inversion scheme, compare well with tidal gauge measurements. The study reveals that the amplitude of the semi-diurnal tide, M_2, decreases, while the amplitude of the diurnal tide, K_1, increases similar to the Helmholtz resonance after the tidal waves propagate from the western Pacific into the SCS through the Luzon Strait (LS). Analyses of the energy studies show that the LS is a place where both M_2 and K_1 tidal energy dissipates the most, and strong M_2 tidal dissipation also occurs in the Taiwan Strait (TS). The work rate of the tidal generating force in the SCS basin is negative for M_2 and positive for K_1. It is found that the responses of tides in the SCS are largely associated with the propagating directions of the tides in the Pacific, the tidal frequency, the wavelengths, the local geometry and bottom topography.
© 2007 Elsevier Ltd. All rights reserved.

Keywords: The South China Sea; Data assimilation; Tide and tidal dynamics

1. Introduction

The South China Sea (SCS) is located between 99E–122E and 0–25N, along the edge of the Eurasian plate. It consists of a deep basin with two continental shelves (about 55% of the total size)

along the north and southwest coasts. In the northern SCS (NSCS), SCS connects to the East China Sea (ECS) through the Taiwan Strait (TS), and to the Pacific Ocean through the Luzon Strait (LS). In the southern part of the basin, it links with the Java Sea through the Karimata Strait, and with the Sulu Sea through several narrow channels between the Philippine Islands (Fig. 1). The complex and steep bottom topography of the SCS has a great influence on the wind-induced circulation and the distribution, propagation and dissipation of the

*Corresponding author at: Department of Mathematics, Hong Kong University of Science and Technology, Clear Water Bay, Kowloon, Hong Kong.

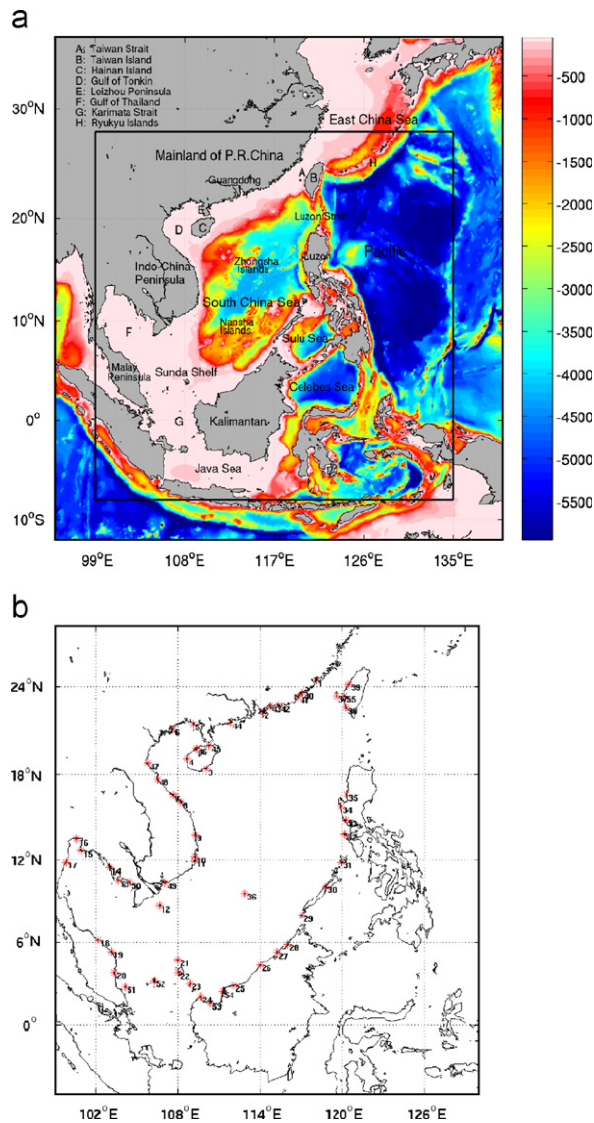*E-mail address:* magan@ust.hk (J. Gan).

Fig. 1. (a) Topography and (b) observation stations in the South China Sea. The area inside the rectangular box in (a) is the model domain of the SCS.

tidal energy. Gan et al. (2006) showed that the seasonal circulation forced by monsoonal wind stress is greatly regulated by the bottom topography along the continental margin. The complicated tidal dynamics over prominent bottom topography has been pointed out in many previous studies (e.g. Morozov, 1995; Egbert and Ray, 2000; Niwa and Hibiya, 2004). These studies found that tidal energy is dissipated not only by the bottom friction in shallow seas but also by scattering of the surface tide over the rough topography into the internal tide.

For the physical process in the SCS, previous studies (e.g. Wyrtki, 1961; Xu et al., 1982; Shaw and Chao, 1994; Chao et al., 1996; Chu et al., 1999; Hu et al., 2000) agreed that the circulation of the SCS is affected mostly by the monsoon winds and that circulation in the NSCS is also related to water exchanges through the LS and the TS. While lower frequency forcing such as heat fluxes and wind stress are dominant factors in ocean circulation on longer time scales, the higher frequency forcing from the tide should not be neglected in reaching a full understanding of the circulation, mass and energy transport, and ecosystem dynamics in the ocean. In addition, the tidal current is also a significant energy source for ocean mixing (Egbert and Ray, 2000), and its energy dissipation accounts for about 1/2 of the mechanical energy needed to maintain the global thermohaline circulation as estimated by Munk and Wunsch (1998).

Based on different data sets, early studies of the tides in the SCS produced cotidal charts that showed great diversity in describing the tidal characteristics in the regions over the continental shelves (e.g. Dietrich, 1944; Sergeev, 1964). Since the 1980s, different approaches have been adopted in tidal studies in the SCS. They include analyzing tidal harmonic constituents from 320 observation stations by Yu (1984), using Topex/Poseidon (T/P) altimetry data by Yanagi et al. (1997) and Hu et al. (2001), and using numerical models by Ye and Robinson (1983) and Fang et al. (1994, 1999). These previous modeling studies all solved the two-dimensional (2D) depth-integrated shallow water equations and applied open boundary conditions to elevation that is determined from estimation of limited local tidal observations or from interpolation of historical cotidal charts. In particular Ye and Robinson (1983) treated the M_2 and K_1 constituents separately in their model. All these studies have shown that tidal waves propagate into the SCS mainly through the LS, and several amphidromic systems exist in the continental shelf areas. The tidal currents are weak and regularly distributed in the deep basin while they are strong and complex on the shelves. Nevertheless, because of the generally adopted low grid resolution with the open boundary on the LS, the previous numerical modeling studies with limited tidal constituents were not well resolved for the tidal dynamics involved in the complex topography in the SCS and the strong tidal energy dissipation in the LS.

The deficiencies in both observation data and numerical equations could be improved by using data assimilation. Both types of information could be used to regulate the behaviors and to correct the errors of the other. The advent of satellite altimetry, which provides us unprecedented amounts of observation data in the ocean, and the development of data assimilation methods in numerical modeling have set up a new venue to tackle these problems. Guided by this concept and considering there is no study of tides that utilized the inverse scheme in a high-resolution model in the SCS so far, we have implemented a high resolution, large nested domain tidal model using a data assimilation method with inversion scheme (Egbert et al., 1994; Egbert and Erofeeva, 2002) in the SCS to investigate the characteristics of the local tide and tidal energy and to explore the dynamics involved in the tidal waves in the SCS, which has been largely neglected in previous studies.

2. Tidal model and its implementation

The OTIS (http://www.coas.oregonstate.edu/research/po/research/tide/index.html Oregon State University Tidal Inversion Software) (Egbert et al., 1994; Egbert and Erofeeva, 2002) is utilized, which consists of prior calculations of dynamic equations and subsequent data assimilation. In the prior calculation, tidal heights and currents are solved by the time stepping, 2D shallow water equations based on the conventional hydrostatic and Bossinesq assumptions, along with the quadratic bottom friction dissipation, inertial terms and horizontal eddy viscosity. The forcing from the astronomical tide generating force, the Earth's body tide, tidal loading and self-attraction are included in the model equations, which consist of a momentum Eq. (2.1) and continuity Eq. (2.2)

$$\frac{\partial \vec{U}}{\partial t} + (\vec{U} \cdot \nabla)\vec{v} + f \times \vec{U}$$
$$+ gH\nabla(\zeta - \zeta_{SAL} - \zeta_E) - HA_h\nabla^2\vec{v} + F = 0, \quad (2.1)$$

$$\frac{\partial \zeta}{\partial t} + \nabla \cdot \vec{U} = 0, \quad (2.2)$$

where H is the water depth, ζ is sea surface elevation, $\vec{v}$ is velocity vector, and $\vec{U}$ is volume transport vector, which equals the velocity vector multiplied by the water depth, H, g is the gravitational acceleration ($9.8 \, \text{m/s}^2$), and $f = 2\Omega \sin \phi$ is the Coriolis parameter, which varies with latitude (Ω is

the earth's rotation rate, ϕ is latitude). The quantity ζ_{SAL} is the ocean self-attraction and loading computed from a global tidal model (Ray, 1998), ζ_E is the combined tidal potential and Earth tide, expressed as $\zeta_E = (1 + k - h)\eta$, with k and h being the standard Love numbers, η is the elevation equilibrium tide, which is given by $\eta_n = H_n \cos^2\phi \cos(\omega_n t + 2\chi + V_n)$, for the semi-diurnal tide, and $\eta_n = H_n \sin 2\phi \cos(\omega_n t + \chi + V_n)$, for the diurnal tide, ϕ is latitude, χ is east longitude, ω_n is the frequency, and V_n is the astronomical argument phase angle. The H_n, k and h values for the eight tidal components are chosen to be the same as those used by Foreman et al. (1993). The quantity A_h is the horizontal viscosity parameter and is set to $100 \, \text{m}^2/\text{s}$. Sensitivity experiments with different horizontal viscosity coefficients (A_h) show that the solutions are not overly sensitive to the values of A_h, although the results with $A_h = 100 \, \text{m}^2/\text{s}$ give smoother solutions. With 10-km spatial resolution and tidal current as large as 1 m/s (around TS), the chosen value of A_h appears to be reasonable. The quantity F is the bottom friction stress expressed as $F = C_D(||u||/H)\vec{U}$, and C_D is set to 0.003. In the assimilation calculation, an efficient generalized inverse (GI) scheme, which is a compromise between hydrodynamic equations and K-dimensional vector of tidal data by minimization of the quadratic penalty functional, is used. The GI scheme is accomplished by a variant of the representer method (Egbert et al., 1994; Egbert, 1997; Egbert and Erofeeva, 2002; Foreman et al., 2004). Since the representer method is not strictly applicable to the non-linear equations mentioned above, a linearized model equation using the time averaged tidal velocity in the quadratic dissipation term (i.e., calculated by $F = C_D(\langle ||u|| \rangle / H)\vec{U}$; here $\langle \rangle$ denotes the time average) and omitting the non-linear term is adopted. Thus, the dynamical equations for data assimilation are linear, and they can be transformed to the frequency domain with individual tidal constituents decoupled.

To minimize the errors from the approximation of the open boundary conditions and more accurately resolve the tides across the LS, the model domain is extended from (0–25N) to (8S–28N) in the south–north direction, and from (99–122E) to (99–135E) in the east–west direction. Since a large amount of the M_2 barotropic tidal energy is dissipated and converts into internal tides along the LS and ECS continental shelf (Egbert and Ray, 2000; Niwa and Hibiya, 2004), moving the eastern

boundary farther away from the LS is expected to give a more accurate representation of the energy distribution and dynamic processes around this area. At the south boundary, because of the spatial complexity and large amplitude of both the diurnal and semi-diurnal tides in the Indonesian Seas (Egbert and Erofeeva, 2002), an optimal southern boundary is chosen along 8S after some sensitivity experiments. Following Egbert et al. (1994) and Egbert and Erofeeva (2002), the errors are allowed in both the open and solid boundaries, and the mass conservation is retained. Tidal transports of the eight major constituents (M_2 S_2 K_1 O_1 N_2 K_2 P_1 Q_1) from the global model solution (TPXO6.2, (($1°/4$) × ($1°/4$)) resolution, obtained from the OSU tidal inverse model output) are applied at all open boundaries. Our model grid size is around 10 km, by far the highest resolution for tidal simulation in the SCS, and the model topography is interpolated from the ETOPO5 (National Geophysical Data Center, NOAA). Model runs for 240 days for the prior calculation and the results of the last 183 days are used in the harmonic analysis. For the data assimilation part, the harmonics from point-wise time series analyses of the T/P altimetry data at all cross-over points with 10 points along-track sites between, obtained during 1992 and 2002, are adopted. The details about the processing and harmonic analyzing of T/P data used in the assimilation could be seen in Egbert and Erofeeva (2002). A total of 214 representers are computed for each constituent, but only 203 are actually used to obtain the inverse solution. The rest of the representers are truncated because of negligible eigenvalues obtained by singular value decomposition (SVD) of the representer matrix. Error calculations have been tested using different de-correlation length scales, and the value of 100 km, which gave the most satisfactory results, is adopted for the dynamical covariance.

3. Characteristics of tides

In this section, the basic tidal characteristics in the SCS are discussed based on the distributions of co-amplitude, co-phase and tidal current ellipses of the tidal constituents generated from the harmonic analysis of the model results. The sea surface elevation, ζ, of any tidal constituent, i, could be expressed as

$$\zeta_i = f_i H_i \cos(\sigma_i t + (V_0 + u)_i - g_i), \qquad (3.1)$$

where f and u are the nodal modulation amplitude and phase corrections, respectively, σ is frequency of tidal constituent i and V_0 is the astronomical argument phase angle. The quantities H and g are the harmonically analyzed constants that represent the maximum amplitude and phase lag, respectively.

3.1. The M_2 tide

The cotidal charts and tidal current ellipses of M_2 are shown in Fig. 2. The co-amplitude and co-phase lines are obtained from H and g in Eq. (3.1). The results show that the M_2 amplitude is generally small (<0.3 m) in the central part of the SCS. In particular, the M_2 amplitudes in the SCS basin, the Gulf of Tonkin and the Gulf of Thailand only reach about 0.2 m. However, the M_2 tide is amplified in the coastal regions with strong shoaling and narrowing effects. The largest M_2 tide amplitude (about 2 m) exists in the TS and the amplitudes of about 1–1.5 m are found in regions south of Guangdong around Leizhou Peninsula, the northwest coast of Kalimantan, south of the Indo-China Peninsula, and around the western and southern parts of the Malay Peninsula. All these places have shallower continental shelves with straits or concave coastlines. Clearly, shoaling and narrowing effects are key factors that increase the M_2 tidal amplitude. The co-phase lines in Fig. 2(a) shows that the M_2 tide propagates mainly from the Pacific into the SCS through the LS, and it is subsequently directed southwestward into the interior of the SCS and northward into the Taiwan shoal. The M_2 tidal amplitude (about 0.2 m) is markedly diminished after passing through the LS from the Pacific (about 0.6 m), which is associated with strong tidal energy dissipation by the local topography (to be discussed in Section 4). The distribution pattern and magnitude of H and g shown in Fig. 2(a) are generally similar to those found by Fang et al. (1999), Hu et al. (2001), and Cai et al. (2006). The component of the southwestward tidal wave bifurcates near Hainan Island, with one propagating into the Gulf of Tonkin and the other continuing southwards to reach the Sunda shelf and form a standing wave in the Gulf of Thailand. The spacing of the co-phase lines demonstrates the wave speed, c, which can be estimated by $c = L/t$, where L is the distance between two neighboring co-phase lines, t is the time needed for the wave to travel this distance, which could be calculated by $t = (\Delta g/360) \times T_{M_2}$,
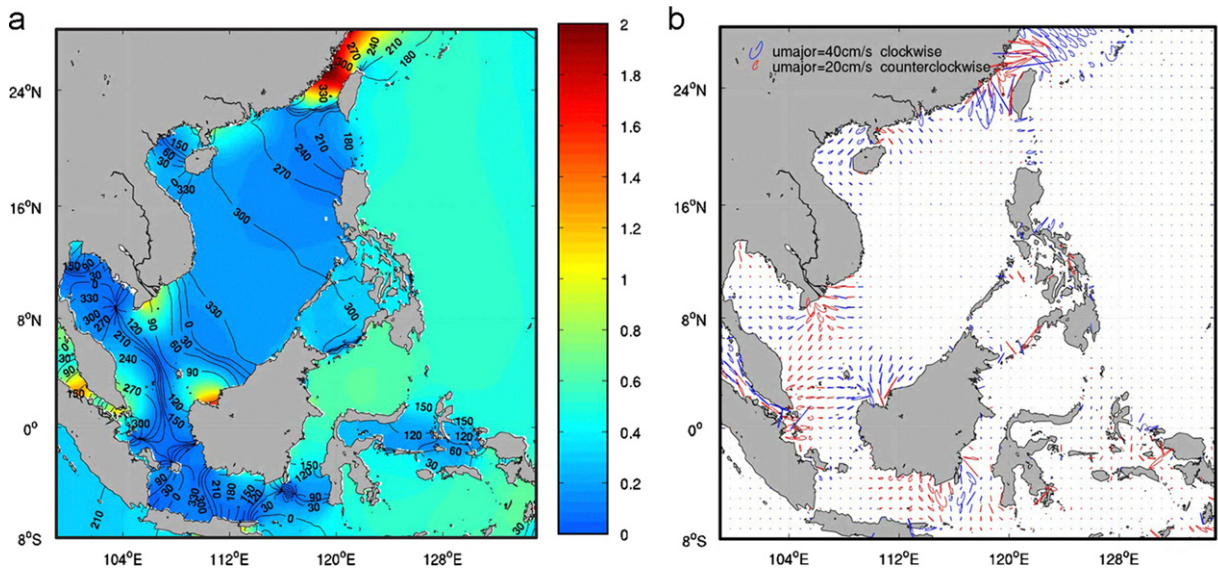
Fig. 2. Cotidal charts and tidal current ellipses of the M_2 tide from the inverse solution. (a) Cotidal charts, (b) tidal current ellipses. Filled contours in (a) denote the magnitude of the co-amplitude (m). Contour lines are the co-phase lines (°) 8 h before GMT at 120°E. Tidal ellipses in (b) are plotted at every eight grid points in both the x- and y-directions.

where Δg is the difference between two neighboring co-phase lines and T_{M_2} is the period of the M_2 tide (for example, in the SCS between 300 and 330 co-phase lines, $\Delta g = 30°$, $T_{M_2} = 12.41\,h$, $t = 3723\,s$, $L \approx 610\,km$, and $c = L/t \approx 164\,m/s$). Obviously, the wave speed for M_2 is large in the SCS basin and small in the continental shelf areas, where the L is much smaller. It is noted that the co-phase lines clustered densely just on the south of the Taiwan shoal along the extension of the 100-m isobath, where the tidal waves propagating northward from the LS and southward from the ECS meet. The interaction of these two waves in the TS (also mentioned by Fang et al. (1999) and Cai et al. (2006)) might contribute to the formation of the largest M_2 tide in the SCS, besides the co-effect from the shoaling of the continental shelf and narrowing of the TS. In the Java Sea, the distribution of the co-phase lines is somewhat irregular compared with the SCS, suggesting a complex tidal system (Egbert and Erofeeva, 2002). We have carried out several sensitivity experiments and found that the tidal results are sensitive to the location of the southern boundary in the Java Sea. Two degenerated counterclockwise amphidrome systems are found on the northern tip of the TS and the northwest of the Gulf of Thailand. A similar degenerated amphidrome point was also found in the northwest of the Gulf of Thailand by

Ye and Robinson (1983) and Cai et al. (2006). However, our degenerated amphidrome point is located farther to the northwest than theirs. The results from Fang et al. (1999) showed an amphidrome point east of our location, instead of a degenerated one. Since the location of the amphidrome point is sensitive to the bottom friction, more precise bottom topography and coastlines are needed to resolve the amphidrome system in shallow waters. A clockwise amphidrome system is found inside the Gulf of Thailand, which is very rare in the northern hemisphere. The right turning of the incident wave and low latitudes can be considered as the main causes, as explained by Fang et al. (1999).

The tidal current ellipses show the velocity vector tracks for one constituent, in which the major axis and minor axis correspond to the maximum and minimum tidal velocity of this constituent, respectively. Fig. 2(b) shows the tidal current ellipses of the M_2 tide, with strong currents in the shallower continental shelves and weak currents in the deep ocean basin. It can be seen clearly that the large tidal currents are found in the places with large tidal amplitude, except at the LS, where relatively large currents with small amplitudes occur. As tidal currents pass the narrow LS, the velocity and thus the kinetic energy increase, while the potential energy decreases in the form of

amplitude decrease according to the Bernoulli conservation theorem.

3.2. The K_1 tide

Similar to the conditions of the M_2 tide, relatively high amplitude of the K_1 tide appears on the continental shelf, particularly the Sunda shelf (Fig. 3(a)). However, unlike M_2 no extremely high amplitude of K_1 exists in the TS, and the largest amplitude of the K_1 tide occurs in the Gulf of Tonkin (about 0.7–0.9 m). Three other areas with relatively high K_1 amplitudes are located on the northern part and mouth of the Gulf of Thailand and south of the Karimata Strait (about 0.6 m). The corresponding strong K_1 currents are found in the Gulfs of Tonkin and Thailand and over the continental shelf in the northern and southwestern parts of the basin (Fig. 3(b)). The K_1 currents are stronger in the gulfs of Tonkin and Thailand, the LS, and the Karimata Strait, but weaker in the TS, as compared with currents induced by the M_2 tide. Note that, contrary to the condition of the M_2 tide, the amplitude of K_1 is markedly increased in the SCS basin (about 0.2–0.4 m) after propagating from the Pacific (about 0.1–0.2 m) through the LS. This particular phenomenon has never been documented before. Since the SCS is separated from Pacific Ocean forcing by LS, the amplified K_1 is considered to be caused by the Helmholtz resonance inside the SCS, given that the phase and amplitude of the K_1 tide in the SCS basin are nearly constant (Fig. 3). According to Sutherland et al. (2005), the resonant frequency for a Helmholtz oscillator, ω_0, is $\omega_0 = \sqrt{gE/Al}$, where l is the length of the LS, A is the surface area of the SCS, and E is the cross-sectional area of the LS. Given $E = 748\,\mathrm{km}^2$, $l = 378\,\mathrm{km}$ and $A = 4 \times 10^6\,\mathrm{km}^2$, we have the resonant period $T_0 = (2\pi/\omega_0) = 24.8\,\mathrm{h}$, which is close to the diurnal tidal periods of K_1 (23.93 h) and O_1 (25.82 h) tides. Similar resonance in the SCS is obtained using an improved formula which integrates along the LS (Garrett and Cummins, 2005). The resonance in the SCS is also found in O_1 (see Fig. 4(b)).

Like the M_2 tide, the K_1 tide mainly propagates into the SCS from the Pacific through the LS (Fig. 3(b)). However, as compared with the M_2 tide, a much weaker tidal diffraction of K_1 occurs around Taiwan Island as it propagates from the Pacific towards the ECS and the SCS. The K_1 tide forms two degenerated counterclockwise amphidrome systems, at the northern tip of Luzon Island and in the southwestern part of the Gulf of Tonkin, and a counterclockwise amphidrome system inside the Gulf of Thailand. The rotation direction of the K_1 tide in the Gulf of Thailand is opposite to that of the M_2 tide, suggesting that the clockwise amphidrome system of M_2 may be due to its particular tidal frequency, although its real mechanism requires
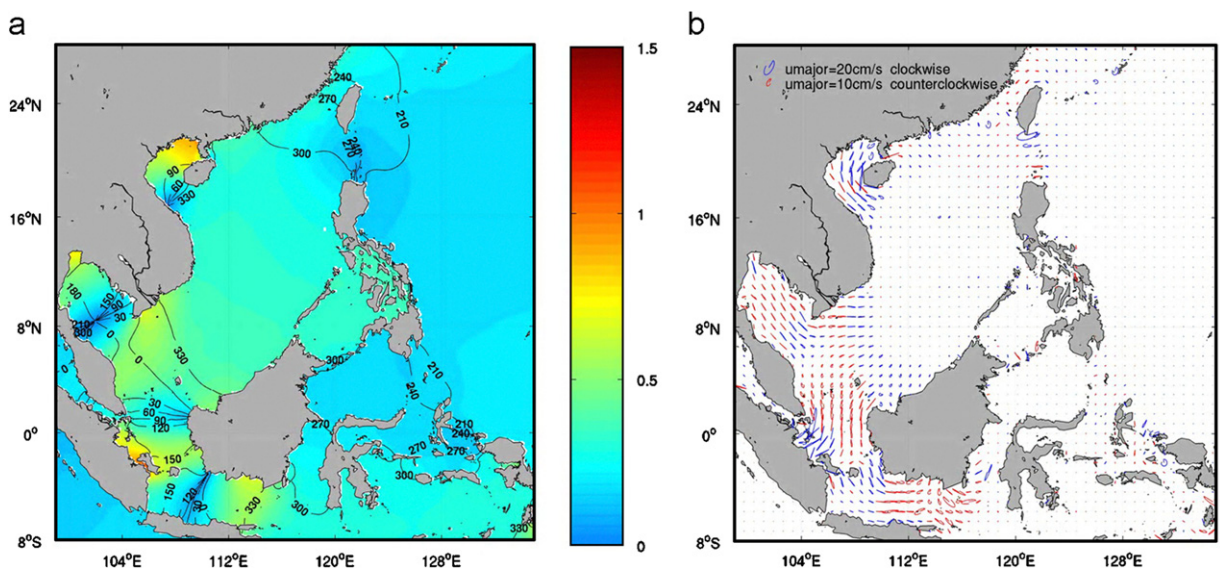

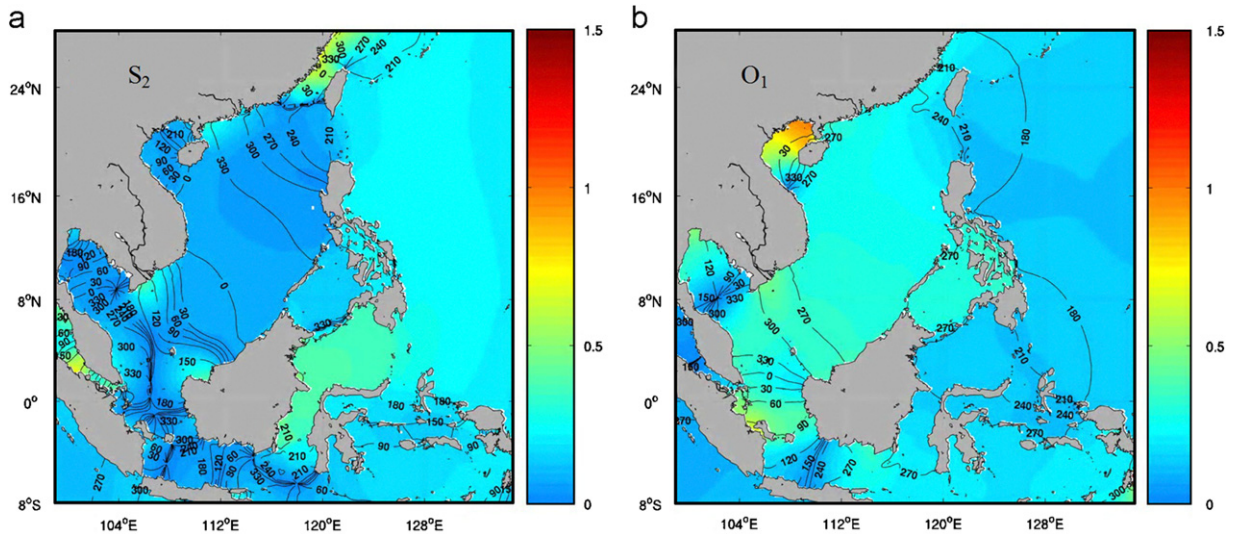Fig. 3. Same as Fig. 2, but for the K_1 tide.

Fig. 4. Inverse results of S_2 and O_1 tide, same as Figs. 2(a) and 3(a).

further investigation. In addition, there are three other distinct differences between the K_1 and M_2 co-phase lines. The first one is that no densely clustered K_1 co-phase lines exist south of the TS, indicating that no K_1 tidal wave turns northward after entering through the LS. The second difference is that the spaces between the co-phase lines of K_1 in the SCS basin are larger than those of M_2. However, it should be noted that the M_2 and K_1 tidal waves, in fact, propagate at almost the same speed after converting the phase lag into the corresponding time lag. The third difference is that after reaching the Sunda shelf, the K_1 tidal wave propagates southward across the Kalimantan Strait and into the Java Sea, while the M_2 tidal wave mainly travels westward (Figs. 2(a) and 3(a)). This difference is also reflected in the tidal current ellipses (Fig. 3(b)), with strong K_1 and weak M_2 currents along the strait. In addition, M_2 rotates clockwise inside the Gulf of Thailand, while K_1 rotates counterclockwise. This is also correlated with the different rotation directions of the amphidrome systems inside the gulf. Obviously, most of these phenomena are closely related to the local bottom topographies and shapes of the gulfs.

3.3. The S_2 and O_1 tides

Similar to results obtained by Fang et al. (1999) and Hu et al. (2001), the S_2 and O_1 tides exhibit similar co-amplitude and co-phase patterns to the M_2 and K_1 tides, respectively (Fig. 4). The amplitude of S_2 is visibly smaller than that of M_2, while the amplitudes of K_1 and O_1 are comparable. Similar to K_1, the O_1 with period of 25.82 h also experiences Helmholtz resonance in the SCS. In addition, we have compared the solutions with those in which only M_2 and K_1 are included in the simulations and found that there is little difference between the solutions with the two and eight constituents included, suggesting that the non-linear interactions among the constituents are weak. A relatively large difference is found in K_1, primarily due to the relative importance of O_1 in this region.

3.4. Comparison with the prior solution

The main procedure of OTIS could be divided into two parts. Results from the first part, i.e., the prior solution ($\vec{U}_0$), are obtained by solving the time-stepping 2D dynamic Eqs. (2.1) and (2.2), then the solution $\vec{U}$, which minimizes the cost function, is the linear combination of $\vec{U}_0$ and the representers (Egbert et al., 1994). To evaluate the performance of the dynamics of the OTIS and the effect from the data assimilation, the model results from the prior solution (without data assimilation) are shown in Fig. 5(a) and (b).

Reasonably good tidal characteristics in the SCS are displayed in the prior solution, suggesting the
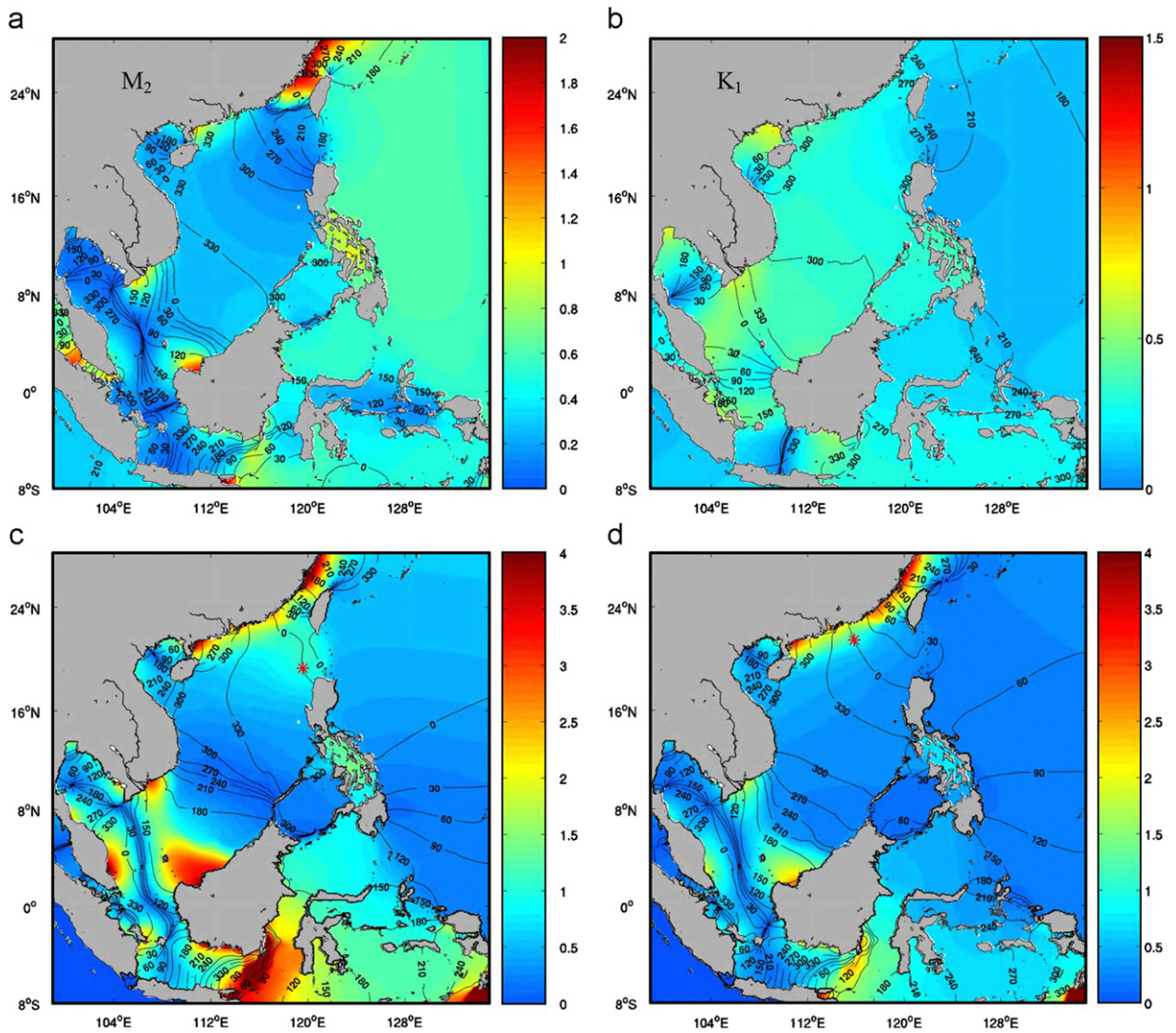
Fig. 5. (a) and (b) Are the same as Figs. 2(a) and 3(a), but for the prior solution. (c) and (d) Are scaled amplitude and phase map of representers for M_2 tide. The asterisk show the location of the representers, filled contours show the scaled amplitude of the representer, and contour lines (deg.) show the corresponding phase lag of the representers in (c) and (d).

correctness of the model dynamics. The roles of data assimilation include corrections to the 2D approximation of the water column, rough parameterization of the complex physical processes and computational errors caused by the differential method. No large difference between prior and inverse results is found for either M_2 or K_1 in the Pacific. However, the corrections for the tides from data assimilation become obvious after the tidal waves enter the SCS through the LS. The most conspicuous one is the position of the $300°$ co-phase line of both M_2 and K_1. In the inverse solution, the

$300°$ co-phase line moves farther southwestward for M_2 and northeastward for K_1, indicating that the tidal wave speed in the SCS increases for M_2 and decreases for K_1 in the inverse solution. Similar to their difference in amplitude changing after passing through the LS, the M_2 and K_1 tides again act differently in the SCS. By assimilating data obtained from altimetry remote sensing, the high tide time for the M_2 tide is brought forward in the SCS deep basin, the TS, the Gulf of Tonkin and the Gulf of Thailand, while it is postponed for the K_1 tide only in the deep basins and the Gulf of Tonkin.

On condition that the errors in the satellite observations are small enough, we could think that the changes between the prior and inverse solutions are caused mainly by the large bottom topography gradient and the coarse parameterization of the bottom friction coefficient. However, the most conspicuous change between the prior and inverse solutions in the SCS basin is probably caused by the inclusion of baroclinicity, i.e., the internal tide in the inverse flow field. Many studies (Jan et al., 2007; Niwa and Hibiya, 2004; Tian et al., 2003; Egbert and Ray, 2000) have pointed out that internal tides are generated in the LS and the continental shelf on the ECS with huge tidal energy dissipation.

Figs. 5(c) and (d) show examples of representer for the M_2 constituent measured at the sites west of the LS and the continental edge of northern shelf, respectively. Following Foreman et al. (2004), the values of amplitudes and phase are scaled with respect to the values of the measured sites. The results at both sites suggest that large amplitudes of the representers are mainly on the shelf, where water is shallow, and in the slope, where topography gradient is large.

3.5. Model results validation

Simulated tidal harmonic constants are compared with those observation data obtained from tidal stations in the SCS. The comparison results for M_2 and K_1 tidal components are listed in Table 1. Differences between their amplitudes and phase lags are calculated as distances in the complex plane (Foreman et al., 1993)

$$d = \sqrt{(H_O \cos g_O - H_S \cos g_S)^2 + (H_O \sin g_O - H_S \sin g_S)^2},$$

where H_O, g_O, H_S and g_S are the observed and simulated amplitudes and phase lags. The RMS error of the complex amplitude is

$$\sqrt{\frac{1}{2N}\sum_{i=1}^{N}|H_{Si} - H_{Oi}|^2},$$

where N is the number of the observation stations, H_{Si} is the model simulated amplitude at station i and H_{Oi} is the amplitude from observation data at station i.

Observation data are those first composed by Fang et al. (1999) and used by Hu et al. (2001) and Cai et al. (2006) based on two sources of data. Data from the stations along the coasts of the mainland of P.R. China, Hainan Island and Yongshujiao taken from the archives of the Institute of Oceanology, the Chinese Academy of Sciences are generally based on at least a full year of observations. The rest of the stations are quoted from the British Admiralty Tide and Tidal Stream Tables, and their data quality varies (Fang et al., 1999). In our computational domain, we randomly selected 55 observation stations from these two sources of data. Simulated harmonic constants at the observation stations are interpolated or extrapolated by those on the nearest model grids. The results are presented in Table 1.

In general, the results obtained in this study with the GI scheme are improved in comparison with the results along these coastal stations from the previous studies. The RMS error of the complex amplitude of M_2 and K_1 for our result is (4.29, 2.15) as shown in Table 1, and were (11.64, 4.39), (17.58, 3.59), (5.01, 2.58) for Fang et al. (1999), Hu et al. (2001), and Cai et al. (2006), respectively. From Table 1 and Figs. 2(a) and 3(a), it is not difficult to discover that most improved stations are focused on the left and right sides of the SCS basin, between 6° and 18°N, where the co-phase lines of both M_2 and K_1 are sparse and their co-amplitude lines do not vary much. The station where the simulation data compares most favorably with the observation data is Yongshujiao (Fig. 6), located south of the central SCS basin (Fig. 1), and where the d of M_2, K_1 are 0.21 and 1.57, respectively. In other words, the tidal waves are well reproduced in the deep basin. However, the results at stations on the shallow continental shelves and in the gulfs, where the accuracy of the tidal wave is highly dependent on the veracity of the coastal topography, are not improved as much as those along basin edges or in the open ocean, as compared with previous results. In general, the model's performance on shallow continental shelves, where the tidal features are complicated, with densely distributed co-phase lines and variable co-amplitude lines, is not as good as that around the deep SCS basin. For example, the d of M_2 and K_1 is 10.62 and 10.92 at Hong Kong, 23.87 and 6.08 at Kuching, much larger than that at Yongshujiao. Insufficient model resolution over the shelves is one of the possible reasons. Since the complex coastlines still could not be well resolved by the present model, small tidal features around the observation stations along the coasts and near the islands might not be represented. In addition,

Table 1
Comparison of the harmonic constant between observation and calculated results

	Station name	Latitude	Longitude	M2									K1								
				Observation		Calculation		Absolute error		Relative error (%)		d	Observation		Calculation		Absolute error		Relative error (%)		d
				H (cm)	g (deg.)	H	g	dH	dg				H	g	H	g	dH	dg			
1	Xiamen	24°27′	118°04′	184	352	168.5	351.3	−15.5	−0.7	8.42	0.20	15.65	34	281	32.2	282.4	−1.8	1.4	5.29	0.50	1.97
2	Hong Kong	22°18′	114°10′	37	256	37.4	272.4	0.4	16.4	1.08	6.41	10.62	36	297	36.2	314.4	0.2	17.4	0.56	5.86	10.92
3	Lingshuijiao	18°23′	110°04′	18	310	19.9	304.9	1.9	−5.1	10.56	1.65	2.54	30	317	32.7	316	2.7	−1	9.00	0.32	2.75
4	Basuo	19°06′	108°37′	18	61	17.6	66.6	−0.4	5.6	2.22	9.18	1.78	54	71	55	74.3	1	3.3	1.85	4.65	3.29
5	Beihai	21°29′	109°05′	44	177	43.1	177.5	−0.9	0.5	2.05	0.28	0.98	88	96	88.1	101.7	0.1	5.7	0.11	5.94	8.76
6	Tsieng mum	21°08′	107°37′	18	179	19.4	173.4	1.4	−5.6	7.78	3.13	2.30	73	96	79.1	101.6	6.1	5.6	8.36	5.83	9.61
7	Thuan An	16°34′	107°38′	18	351	19.1	350.5	1.1	−0.5	6.11	0.14	1.11	3	270	4.2	302.4	1.2	32.4	40.00	12.00	2.32
8	Da Nang	16°05′	108°11′	17	330	17	319.2	0	−10.8	0.00	3.27	3.20	20	304	23.6	301.8	3.6	−2.2	18.00	0.72	3.70
9	Qui Nhon	13°45′	109°13′	18	321	17.5	312.3	−0.5	−8.7	2.78	2.71	2.74	34	315	32.7	311.4	−1.3	−3.6	3.82	1.14	2.47
10	Nha Trang	12°12′	109°12′	18	321	17.9	317.9	−0.1	−3.1	0.56	0.97	0.98	34	307	33.8	311.8	−0.2	4.8	0.59	1.56	2.85
11	Cam Ranh	11°53′	109°12′	18	329	18.5	320	0.5	−9	2.78	2.74	2.91	34	307	34.3	311.3	0.3	4.3	0.88	1.40	2.58
12	Con Dao	8°40′	106°38′	79	81	71	82.9	−8	1.9	10.13	2.35	8.38	64	333	59	339.7	−5	6.7	7.81	2.01	8.75
13	Ream	10°30′	103°36′	7	29	6.4	12.8	−0.6	−16.2	8.57	55.86	1.98	22	135	19.7	124.8	−2.3	−10.2	10.45	7.56	4.36
14	KaohKong Is.	11°25′	103°00′	12	51	9.4	24	−2.6	−27	21.67	52.94	5.60	37	161	34.7	161	−2.3	0	6.22	0.00	2.30
15	Satahib bay	12°39′	100°55′	24	159	21	160.5	−3	1.5	12.50	0.94	3.06	64	176	62.5	180.7	−1.5	4.7	2.34	2.67	5.40
16	Bangkok bar	13°28′	100°35′	55	170	40.7	184.7	−14.3	14.7	26.00	8.65	18.74	67	182	73.3	188.7	6.3	6.7	9.40	3.68	10.33
17	Ko Reat	11°48′	99°49′	6	168	6.8	170.3	0.8	2.3	13.33	1.37	0.84	52	184	52.1	181.8	0.1	−2.2	0.19	1.20	2.00
18	Tumpat	6°12′	102°10′	18	261	16.2	247.3	−1.8	−13.7	10.00	5.25	4.45	28	351	25.3	346.8	−2.7	−4.2	9.64	1.20	3.33
19	Trengganu	5°21′	103°08′	27	243	26.3	237.4	−0.7	−5.6	2.59	2.30	2.70	52	3	48.8	1.4	−3.2	−1.6	6.15	53.33	3.50
20	Kuantan	3°50′	103°20′	55	270	55.19	262	0.19	−8	0.35	2.96	7.69	52	18	52.4	13.4	0.4	−4.6	0.77	25.56	4.21
21	Pulau Laut	4°45′	108°00′	9	85	14.7	80.4	5.7	−4.6	63.33	5.41	5.77	36	348	41.5	343	5.5	−5	15.28	1.44	6.45
22	Natuna	3°48′	108°02′	21	117	21	106.9	0	−10.1	0.00	8.63	3.70	40	355	36.5	352.9	−3.5	−2.1	8.75	0.59	3.77
23	Subi Kechil	3°03′	108°51′	49	109	44.9	103.8	−4.1	−5.2	8.37	4.77	5.91	37	350	35.5	344.1	−1.5	−5.9	4.05	1.69	4.02

24	Tangjong Datu	2°05′	109°39′	91	117	113.2	117.1	22.2	0.1	24.40	0.09	22.20	37	335	45.6	340.4	8.6	5.4	23.24	1.61	9.43
25	Batang Mukah	2°54′	112°05′	37	93	33.9	88.2	−3.1	−4.8	8.38	5.16	4.29	40	326	44.1	323.9	4.1	−2.1	10.25	0.64	4.38
26	Miri	4°23′	113°59′	15	341	15.8	335.7	0.8	−5.3	5.33	1.55	1.63	37	324	36.9	315.3	−0.1	−8.7	0.27	2.69	5.61
27	Labuan	5°17′	115°15′	27	322	26	322.8	−1	0.8	3.70	0.25	1.07	40	320	38.2	317.3	−1.8	−2.7	4.50	0.84	2.58
28	Kota Kinabalu	5°52′	115°59′	23	314	27.7	325.9	4.7	11.9	20.43	3.79	7.03	35	314	37.7	318.8	2.7	4.8	7.71	1.53	4.07
29	Balabak Is.	8°00′	117°04′	24	314	21.3	311.6	−2.7	−2.4	11.25	0.76	2.86	30	323	34.2	314.3	4.2	−8.7	14.00	2.69	6.42
30	Ulugan bay	10°04′	118°46′	21	304	19.4	303.4	−1.6	−0.6	7.62	0.20	1.61	34	317	31.8	313.6	−2.2	−3.4	6.47	1.07	2.94
31	Kulion Is.	11°48′	119°57′	24	303	23.5	300.9	−0.5	−2.1	2.08	0.69	1.00	30	318	31.9	317.2	1.9	−0.8	6.33	0.25	1.95
32	Lubang Is.	13°49′	120°12′	20	290	16.5	292	−3.5	2	17.50	0.69	3.56	29	310	29.1	313.3	0.1	3.3	0.34	1.06	1.68
33	Olongapo	14°49′	120°17′	17	287	15.2	290.1	−1.8	3.1	10.59	1.08	2.00	27	316	28.3	313.8	1.3	−2.2	4.81	0.70	1.68
34	Santa Cruz	15°46′	119°54′	12	263	12.8	285.3	0.8	22.3	6.67	8.48	4.86	26	313	26.9	314	0.9	1	3.46	0.32	1.01
35	San Fernando	16°37′	120°18′	8	264	9.5	268.3	1.5	4.3	18.75	1.63	1.64	24	312	23.5	315.2	−0.5	3.2	2.08	1.03	1.42
36	Yongshujiao	9°33′	112°53′	18	319	17.8	318.9	−0.2	−0.1	1.11	0.03	0.20	35	311	34.3	313.4	−0.7	2.4	2.00	0.77	1.61
37	Makung	23°23′	119°34′	87	326	95.8	326.2	8.8	0.2	10.11	0.06	8.81	25	278	24.5	276.8	−0.5	−1.2	2.00	0.43	0.72
38	Kaohsiung	22°37′	120°16′	15	236	19.9	211.7	4.9	−24.3	32.67	10.30	8.77	16	295	18.5	283	2.5	−12	15.63	4.07	4.38
39	Taichung	24°11′	120°29′	148	327	163.8	317.8	15.8	−9.2	10.68	2.81	29.55	18	268	23.4	264.5	5.4	−3.5	30.00	1.31	5.54
40	Shaoanwan	23°36′	117°06′	76	14	76.5	14.71	0.5	0.71	0.66	5.07	1.07	34	292	30.7	291.2	−3.3	−0.8	9.71	0.27	3.33
41	Shantou	23°20′	116°45′	41	22	45.1	16.12	4.1	−5.88	10.00	26.73	6.02	29	297	29.3	292.2	0.3	−4.8	1.03	1.62	2.46
42	Shanwei	22°45′	115°21′	28	255	25	246.5	−3	−8.5	10.71	3.33	4.94	33	298	32.4	296.3	−0.6	−1.7	1.82	0.57	1.14
43	Dayawan	22°44′	114°44′	37	252	36.8	253.1	−0.2	1.1	0.54	0.44	0.74	34	295	36.1	302.8	2.1	7.8	6.18	2.64	5.21
44	Hailingshan	21°35′	111°49′	68	294	54.6	276	−13.4	−18	19.71	6.12	23.30	42	314	38.7	312.7	−3.3	−1.3	7.86	0.41	3.42
45	Haikou	20°01′	110°17′	20	264	23.9	253.2	3.9	−10.8	19.50	4.09	5.67	39	96	36.7	91.2	−2.3	−4.8	5.90	5.00	3.92
46	Yangpu	19°50′	109°20′	24	150	29	148.7	5	−1.3	20.83	0.87	5.04	73	85	78.9	90.8	5.9	5.8	8.08	6.82	9.68
47	Hon Nieu	18°48′	105°46′	30	31	37.7	32.1	7.7	1.1	25.67	3.55	7.73	49	103	51	110.5	2	7.5	4.08	7.28	6.84
48	Quang Khe	17°42′	106°28′	18	41	25.3	17	7.3	−24	40.56	58.54	11.49	21	110	25	107.1	4	−2.9	19.05	2.64	4.16
49	Vung Tau	10°20′	107°04′	79	63	69.7	65.1	−9.3	2.1	11.77	3.33	9.69	61	327	55.6	327.5	−5.4	0.5	8.85	0.15	5.42
50	Hatien	10°22′	104°28′	10	119	13	98.2	3	−20.8	30.00	17.48	5.09	26	81	23	79.5	−3	−1.5	11.54	1.85	3.07
51	Pulau Tionman	2°48′	104°08′	58	274	62.9	272.7	4.9	−1.3	8.45	0.47	5.09	49	25	46.6	25.3	−2.4	0.3	4.90	1.20	2.41
52	Anamba Is.	3°14′	106°15′	18	267	17.3	256.7	−0.7	−10.3	3.89	3.86	3.24	40	13	39	13.4	−1	0.4	2.50	3.08	1.04
53	Kuching	1°34′	110°21′	149	131	150.9	121.9	1.9	−9.1	1.28	6.95	23.87	47	348	48.7	341	1.7	−7	3.62	2.01	6.08
54	Kuala Paloh	2°27′	111°14′	110	114	116.7	117.8	6.7	3.8	6.09	3.33	10.07	46	338	46.5	336.3	0.5	−1.7	1.09	0.50	1.46
55	Putai	23°23′	120°09′	60	312	62.1	307.8	2.1	−4.2	3.50	1.35	4.94	20	278	20.4	274.3	0.4	−3.7	2.00	1.33	1.36
averarge absolute error								0.46	−3.81								0.43	0.31			
RMS error of complex amplitude								4.29									2.15				

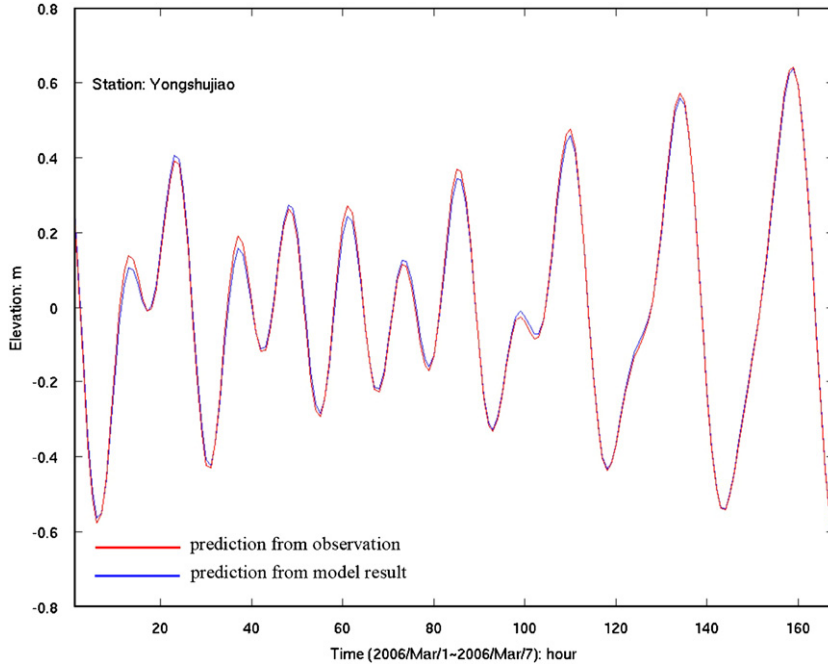g is the local phase lag, 8 h before GMT at 120°E.

Fig. 6. Tidal elevation predictions from the model results and the observation data based on M_2 S_1 K_1 and O_1 constituents for the Yongshujiao station.

omitting non-linear terms in the data assimilation part might also compromise the accuracy of the model results, as non-linear interactions between tidal constituents are sometimes important in shallow waters. The figures in Table 1 also show that the results for K_1 are better than those for M_2 in the TS, because the strong M_2 tide is highly sensitive to the local topography. On the contrary, results for M_2 are better than those for K_1 at the northern part of the Gulf of Tonkin.

4. Tidal energy and dynamic discussion

To understand the tidal dynamics and to explain the mechanism of the processes of the M_2 and K_1 tides, the distribution of tidal energy in the SCS is investigated in this section. Following Garrett (1975), the energy equation is obtained by the non-linear equations in the prior model. Adding (2.1)$\vec{v}$ and (2.2)$g\zeta$, we have

$$\frac{\partial E}{\partial t} + \nabla \cdot (g\vec{U}\zeta) = g\vec{U} \cdot \nabla(\zeta_{SAL} + \zeta_E) - F \cdot \vec{v} - (\vec{U} \cdot \nabla\vec{v}) \cdot \vec{v}$$
$$+ HA_h\vec{v} \cdot \nabla^2\vec{v}, \qquad (4.1)$$

where $E = (1/2)H\vec{v}^2 + (1/2)g\zeta^2$ denotes the energy density. Assuming that $\partial E/\partial t = 0$ and (4.1) $\times \rho$ and

averaged over a tidal cycle, then (4.1) becomes

$$W - \nabla \cdot P = D + N - L, \qquad (4.2)$$

where $W = \rho g \langle U \cdot \nabla(\zeta_{SAL} + \zeta_E) \rangle$ is the work rate done by the tidal generating force, $P = \rho g \langle U\zeta \rangle$ denotes the tidal energy flux, $\nabla \cdot P$ represents the divergence of the energy flux, $D = \rho \langle F \cdot \vec{v} \rangle$ denotes the tidal dissipation rate caused by the bottom friction, $N = (\vec{U} \cdot \nabla\vec{v}) \cdot \vec{v}$ is the work rate by the non-linear interaction, $L = HA_h\vec{v} \cdot \nabla^2\vec{v}$ is the dissipation caused by the lateral friction, and $\langle \ \rangle$ denotes time average.

In the data assimilation calculation, the energy Eq. (4.2) can be written as

$$W - \nabla \cdot P = D + N + L + D', \qquad (4.3)$$

where D' denotes the residuals in the momentum equation. When the numerical techniques are assumed reasonably accurate, D' is mostly due to the incomplete and inaccurate physics prescribed in the dynamic equation, probably arising from some uncertain dissipation processes, such as the energy transformation from barotropic tide into the internal tide, etc. Other terms are the same as those in Eq. (4.2).

4.1. Tidal energy distribution

The values of P, $\nabla \cdot P$ and W calculated from (4.3) are shown in Figs. 7–9, respectively. From Fig. 7, we could see that southeast of LS in the Pacific; the directions of the M_2 and K_1 tidal energy flux are quite different. The M_2 energy fluxes are northward and northwestward, while the K_1 energy fluxes are southwestward. In the northeast of the LS, the tidal energy fluxes of both M_2 and K_1 are amplified as the tidal waves approach the 3000-m isobath from the open ocean. The directions of P for both M_2 and K_1 shift southwestward by the southwest–northeast oriented isobaths northeast of the TS. Only the stronger M_2 energy flux is able to cross this topographical trench (Ryukyu trench) and propagates northward into the ECS, while the energy flux of K_1 is guided mainly by the
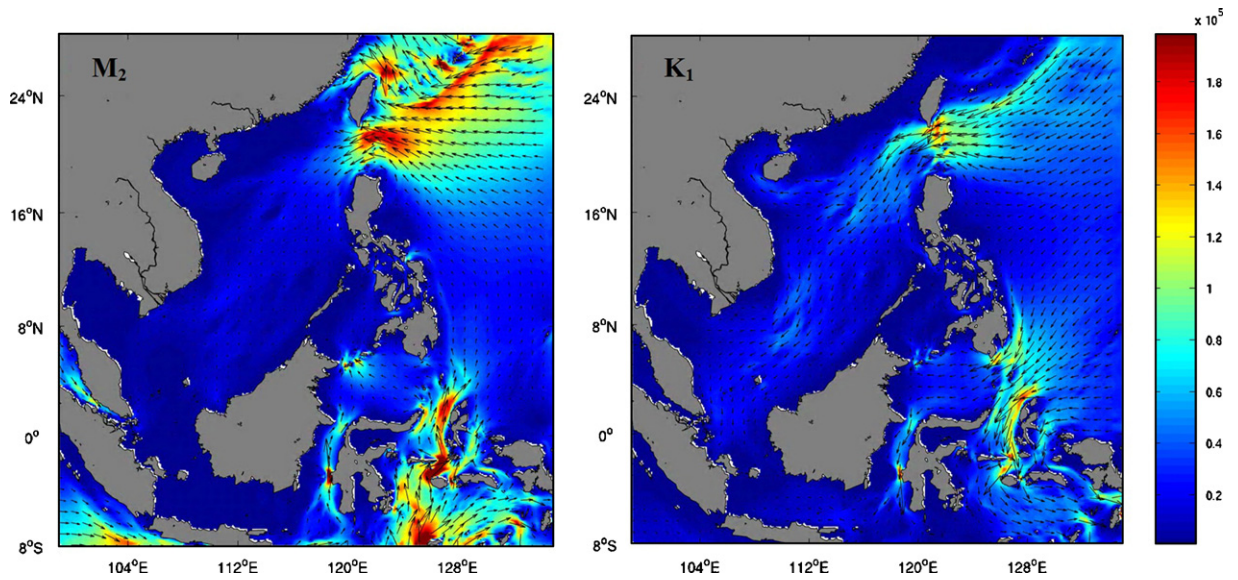
Fig. 7. Vectors of tidal energy flux (P) for M_2 and K_1. Contours denote the magnitude of P (W/m).
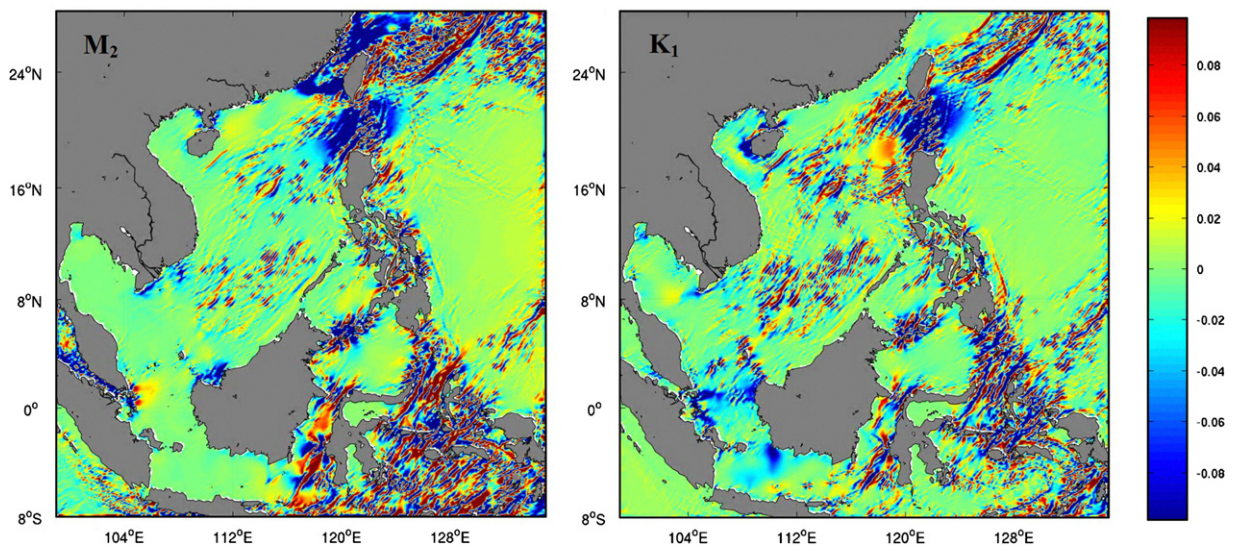
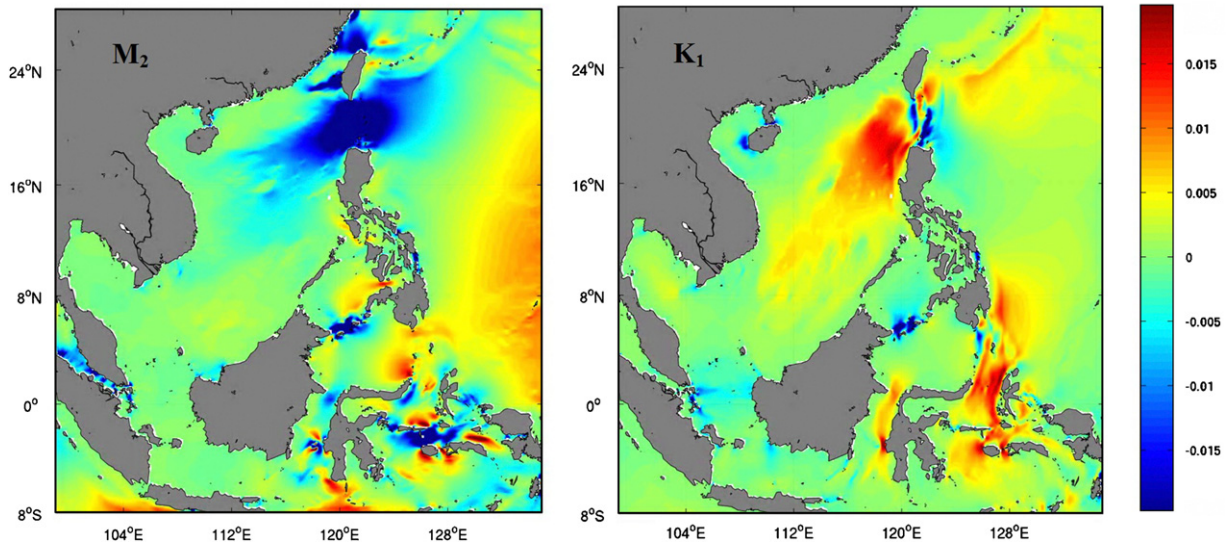Fig. 8. Divergence of the tidal energy flux, $\nabla \cdot P$ (W/m^2).

Fig. 9. The work rate done by the tidal generating force, W (W/m^2).

local topography and propagates southwestward. The maximum M$_2$ and K$_1$ energy fluxes reach 2×10^5 and 1.5×10^5 W/m, respectively, in the LS, and the westward vectors of both the M$_2$ and K$_1$ energy fluxes suggest that the energy fluxes enter the SCS from the Pacific through the LS. On the east side of the LS, the magnitude of both M$_2$ and K$_1$ tide energy fluxes are larger than those on the west side of the LS, indicating the loss of energy while tidal waves passing through the LS. In addition, only M$_2$ energy flux is able to intrude into the SCS through the TS. Inside the SCS, both tidal waves propagate southwestward, which are in accordance with the cotidal charts. However, the magnitude of the M$_2$ energy flux is weaker than that of K$_1$ inside the SCS, while the opposite state occurs around the east of and in the LS.

The different characteristics of the M$_2$ and K$_1$ energy fluxes are associated with the work rate of the tidal generating force, energy divergence and dissipation around the LS, and with the directions of the tidal energy flux east of the LS affected by the existence of the northeast–southwest oriented steep Ryukyu trench. The divergence of the tidal energy fluxes is tightly correlated with the bottom topography (Fig. 8), as shown by the concomitant appearance of the strong energy flux divergence and convergence over the complex and sharply changed topography, such as the Ryukyu trench northeast of Taiwan, the narrow steep straits and the Zhongsha,

Nansha archipelago inside the SCS basin. Fig. 8(a) shows that the LS and the TS are two regions with the strongest M$_2$ energy flux convergence. The values of $\nabla \cdot P$ in these two regions are more than -0.1 W/m^2, about five times of the values of W (see below). According to (4.3), it suggests that strong M$_2$ tidal energy dissipation occurs in the LS and the TS. Since the LS is also a main convergent zone for the K$_1$ tidal energy flux (Fig. 8(b)), it could be regarded as a pump that absorbs and dissipates the tidal energy coming from the Pacific. On the west side of the LS in the SCS basin, there exists a relatively large convergent/divergent area (about 0.03–0.06 W/m^2) of the M$_2$/K$_1$ tides, with the existence of the larger negative/positive work rate in the area (Fig. 9), suggesting that the M$_2$/K$_1$ tidal energy is reduced/amplified in this region.

A positive W denotes energy gain from the work of the tidal generating force, and a negative W denotes energy loss while work is done against the tidal generating force. Fig. 9 shows that W is near zero on most of the continental shelves. A large area of positive work rate of the M$_2$ tidal generating force, W, occurs in the Pacific basin (about 0.003–0.01 W/m^2). The areas of positive W for the K$_1$ tide in the Pacific are smaller than that for M$_2$, and mainly located along the 3000-m isobath east of Taiwan, where negative W is dominant for M$_2$. The amplified negative value (about -0.02 W/m^2) of the

M_2 work rate occurs around the LS and in both the northern and southern parts of the TS, suggesting that considerable M_2 energy is lost there to the tidal generating force. The W distribution for the K_1 tide in the LS is closely related to the bottom topography. Regions with negative work rates are found in the shallower areas, while those with positive work rates exist in the deep channel between the two shallower areas. West of the LS in the SCS basin, W is negative for M_2 and positive for K_1. The maximum value of W for K_1 is over $0.015\,W/m^2$. Without showing the distribution of W Ye and Robinson (1983) pointed out that the work done by tidal generating force in the SCS was negative for both M_2 and K_1, while Fang et al. (1999) showed that the W in the SCS basin was negative for M_2 and positive for K_1, in accordance with our results. The spatial distribution of W around the LS also suggests that while propagating from east of the LS into the SCS, the M_2 tide continuously loses energy, and the K_1 tide gains energy from the tidal generating force except in the two small shallower areas in the LS. Therefore, the contrary behavior of the work rate of M_2 and K_1 tidal generating forces might be another factor that explains why M_2 and K_1 tides act quite differently inside the SCS.

The distribution of bottom friction dissipation, D, has also been calculated for the M_2 and K_1 tide (not shown). The results show strong D in shallow areas with large tidal currents, such as in the TS for M_2 and in the gulf of Tonkin for K_1, which is closely related to the distribution of tidal current ellipses shown in Figs. 2(b) and Fig. 3(b). However, no large area of strong D is seen in LS. Since the magnitudes of N and L are 2–3 times smaller than $\nabla \cdot P$, the large energy dissipation (as defined in Egbert and Ray (2000), i.e. $W - \nabla \cdot P$) in the LS is mostly balanced by D' in (4.3), and it could be considered as the correction to the prior model, which could not take into account the conversion of barotropic tidal energy into internal tide.

Additional information about the tide energy can be obtained by comparing the energy flux results from the prior and inverse model. The obvious differences are found in the region around the LS (Fig. 10). The magnitudes of tidal energy fluxes of both M_2 and K_1 in the prior results reaching the LS from the Pacific are weaker than those from the inverse results, but the opposite conditions occur on the west side of the LS. This evidently suggests that more energy of M_2 and K_1 is lost after crossing the

LS when the inverse scheme is applied. Quantitatively, the energy budget across LS is estimated by the energy flux into/out of the box shown in Fig. 10(a). The box is divided into SCS (left box) and Pacific (right box) parts by the central dashed line, representing energy going out of and coming into the box. In the inverse (prior) calculation, for M_2 tide, 48.71 (41.79) GW energy flows into the right box, and 26.05 (35.20) GW energy flows out of the left box, with 22.66 (6.59) GW being dissipated in LS. For K_1 tide, 44.10 (28.48) GW energy flows into the right box, and 19.17 (24.79) GW energy flows out of the left box, with 23.93 (3.69) GW being dissipated in LS. It is obvious that much more energy is dissipated in LS in the inverse calculation. One possible explanation is the conversion of the barotropic tides into the internal tides in the inverse results (Egbert, 1997; Egbert and Ray, 2000; Niwa and Hibiya, 2004). From another point of view, to better understand the dynamic process of tides in areas of such complex topography as the LS, a three-dimensional (3D) model is required. From the above analyses, it is conceivable that the weakened tide energy flux in the SCS after crossing the LS is caused mainly by the strong tidal dissipation occurring in the strait for K_1 and the co-effect of energy lost in working against W and strong tidal dissipation for M_2.

5. Summary

To study the tide and tidal energy in the SCS, T/P altimetry data have been assimilated into a barotropic ocean tide model by using OTIS. It solves the non-linear shallow water equation by time stepping to get the prior results and then it linearizes the equations and uses the advanced GI method in the data assimilation calculation to get the inverse results. The combination of large amounts of T/P data with the dynamically well-defined equations are a good way to improve the accuracy of tidal modeling by diminishing problems such as the uncertainties in shallow waters and coastal areas caused by analyzing only the T/P data and the inaccuracies caused by merely solving the dynamic equations with rough parameterization of the coefficients. Additionally, high resolution and large model domain are applied in our study, which also improve the accuracy of the modeling. Reasonably good results are thereby obtained.

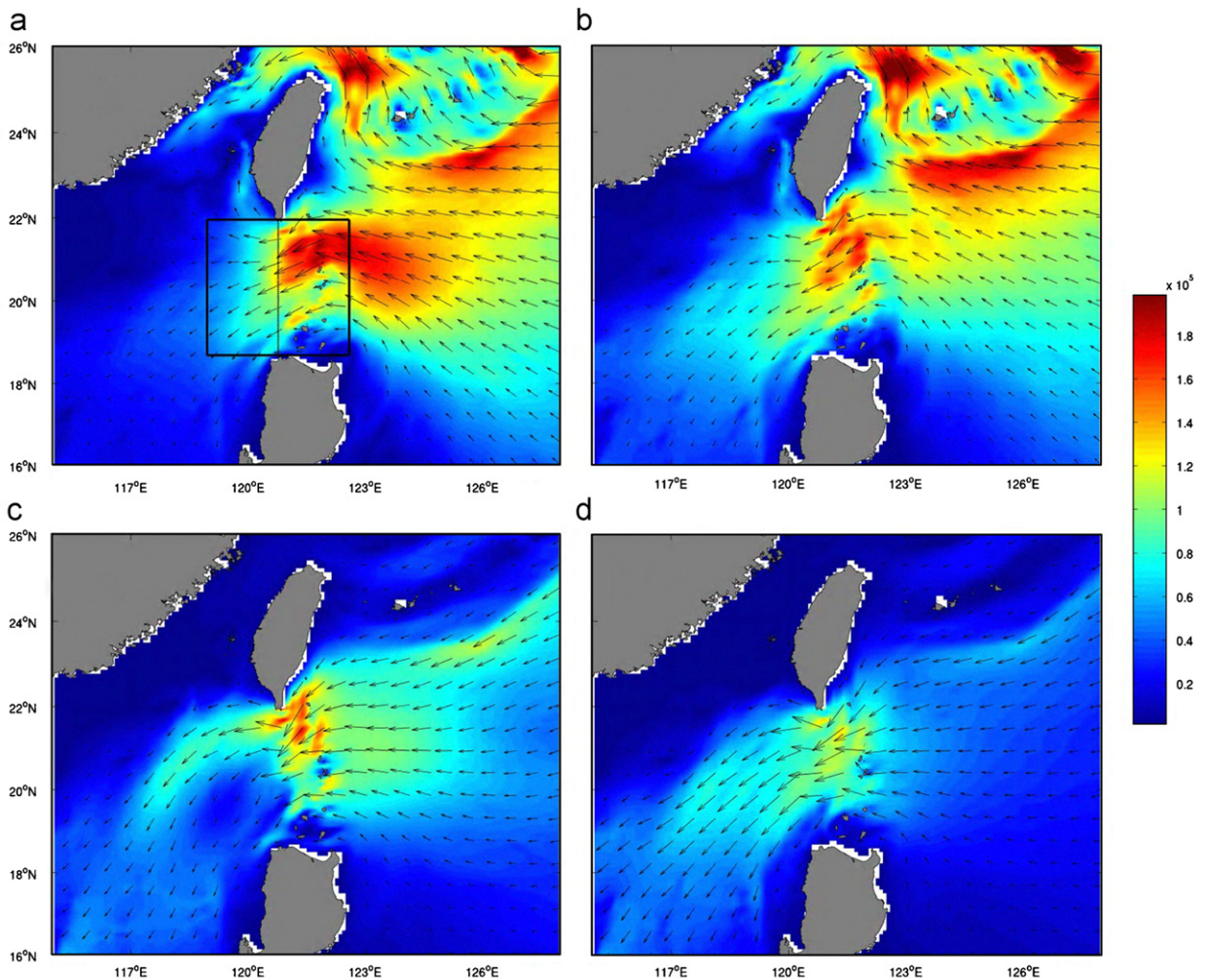Results show that the M_2 and K_1 tides propagate into the SCS through the LS and that they mainly

Fig. 10. The tidal energy flux at the Luzon Strait, (a) the inverse and (b) the prior results for M_2. Similarly, (c) and (d) are for K_1. Contours denote the magnitude of P (W/m).

continue propagating southwestward along the axis of the SCS basin. The M_2 tidal amplitude is reduced while the K_1 amplitude is amplified after they pass through the LS, mainly because of the Helmholtz resonance. The tidal amplitude distribution and the current fields are also closely related to the bottom topography. Tidal characteristics are quite different on the shallow continental shelves and in the deep waters. The tidal waves propagate fast in the deep ocean and slow on the continental shelves, while the tidal currents are strong and complex on the shelf areas and weak and regular in the deep waters. The co-phase lines are rather complex in shallow areas; several amphidromic systems exist on the continental shelf areas and in the two gulfs. Energy

studies show that on the eastern side of Luzon in the Pacific, the northwestward M_2 energy flux is favorable for the intrusion into the ECS, while the southwestward K_1 energy flux is favorable for the intrusion into the SCS. Furthermore, the studies reveal that the magnitudes of the work rate of the tidal generating forces, the divergence of the energy flux and the energy dissipation are amplified in the LS and the TS. Both M_2 and K_1 tidal energies are dissipated most in the LS over the sharply varied bottom topography, indicating the strong control of the topography over the tidal energy distribution. The work rate from the tidal generating force in the SCS basin is negative for M_2 and positive for K_1. The strong

negative W of M_2 in the LS also explains why so much M_2 energy is lost while the tide passes through the LS into the SCS. It can be summarized that the different features of M_2 and K_1 in the SCS are highly associated with the different directions of energy flux in the Pacific, which is unfavorable for the intrusion of M_2 tidal energy into the SCS but favorable for the K_1 tide; and with the tidal energy losses in M_2 and gains in K_1 from W inside the SCS basin. The different M_2 and K_1 behaviors in the SCS are also largely associated with the Helmholtz resonance in K_1.

Acknowledgments

References

Cai, S., Long, X., Liu, H., Wang, S., 2006. Tide model evaluation under different conditions. Continental Shelf Research 26 (2006), 104–112.

Chao, S.Y., Shaw, P.T., Wu, S.Y., 1996. Deep water ventilation in the South China Sea. Deep-Sea Research I 43 (4), 445–466.

Chu, P.C., Edmons, N.L., Fan, C.W., 1999. Dynamical mechanisms for the South China Sea seasonal circulation and thermohaline variability. Journal of Physical Oceanography 29, 2971–2989.

Dietrich, G., 1944. Die Gezeiten des Weltmeeres als geograph, Erseheinung Z. d. ges. Erdkunde, Berlin, 69pp.

Egbert, G.D., 1997. Tidal data inversion: interpolation and inference. Progress in Oceanography 40, 81–108.

Egbert, G.D., Erofeeva, S.Y., 2002. Efficient inverse modeling of barotropic ocean tides. Journal of Atmospheric and Oceanic Technology 19 (2), 183–204.

Egbert, G.D., Ray, R.D., 2000. Significant dissipation of tidal energy in the deep ocean inferred from satellite altimeter data. Nature 405, 775–778.

Egbert, G.D., Bennett, A.F., Foreman, M.G.G., 1994. TOPEX/Poseidon tides estimated using a global inverse model. Journal of Geophysical Research 99, 24821–24852.

Fang, G., Cao, D., Huang, Q., 1994. Numerical modeling of the tide and tidal current in the South China Sea. Acta Oceanologica Sinica 16 (4), 1–12 (in Chinese).

Fang, G., Kwok, Y.K., Yu, K., Zhu, Y., 1999. Numerical simulation of principal tidal constituents in the South China Sea, Gulf of Tonkin and Gulf of Thailand. Continental Shelf Research 19, 845–869.

Foreman, M.G.G., Henry, R.F., Walters, R.A., Ballantyne, V.A., 1993. A finite element model for tides and resonance along the north coast of British Columbia. Journal of Geophysical Research 98, 2509–2531.

Foreman, M.G.G., Sutherland, G., Cummins, P.F., 2004. M_2 tidal dissipation around Vancouver Island: an inverse approach. Continental Shelf Research 24 (2004), 2167–2185.

Gan, J., Li, H., Curchitser, E. N., Haidvogel, D. B., 2006. Modeling South China Sea circulation: response to seasonal forcing regimes. Journal of Geophysical Research 111, C06034, doi:10.1029/2005JC003298.

Garrett, C., 1975. Tides in gulfs. Deep-Sea Research 22, 23–35.

Garrett, C., Cummins, P., 2005. The power potential of tidal currents in channels. Proceedings of the Royal Society. doi:10.1098/rspa.2005.1494.

Hu, J.Y., Kawamura, H., Hong, H., Qi, Y.Q., 2000. A review on the currents in the South China Sea: seasonal circulation, South China Sea warm current and Kuroshio intrusion. Journal of Oceanography 56, 607–624.

Hu, J.Y., Kawamura, H., Hong, H.S., Kobashi, F., 2001. Tidal features in the China Sea and their adjacent sea areas as derived from TOPEX/POSEIDON altimeter data. Chinese Journal of Oceanology and Limnology 19 (4), 293–305.

Jan, S., Chern, C.-S., Wang, J., Chao, S.-Y., 2007. Generation of diurnal K1 internal tide in the Luzon Strait and its influence on surface tide in the South China Sea, Journal of Geophysical Research 112, C06019, doi:10.1029/2006JC004003.

Morozov, E.G., 1995. Semidiurnal internal wave global field. Deep-Sea Research I 42, 135–148.

Munk, W.H., Wunsch, C., 1998. Abyssal recipes II: energetics of tidal and wind mixing. Deep-Sea Research I 45, 1977–2010.

Niwa, Y., Hibiya, T., 2004. Three-dimensional numerical simulation of M_2 internal tides in the East China Sea, J. Geophysical Research 109 (C04027).

Ray, R.D., 1998. Ocean self-attraction and loading in numerical tidal models. Marine Geodesy 21, 181–192.

Sergeev, J.N., 1964. The application of the method of marginal values for the calculation of charts of tidal harmonic constants in the South China Sea. Okeanologiia 4, 595–602 (in Russian, English abstract).

Shaw, P.T., Chao, S.Y., 1994. Surface circulation in the South China Sea. Deep-Sea Research I 40 (11/12), 1663–1683.

Sutherland, G., Garrett, C., Foreman, M.G.G., 2005. Tidal resonance in Juau de Fuca Strait and the Strait of Georgia. Journal of Physical Oceanography 35, 1279–1286.

Tian, J., Zhou, L., Zhang, X., Liang, X., Zheng, Q., Zhao, W., 2003. Estimates of M2 internal tide energy fluxes along the margin of Northwestern Pacific using TOPEX/POSEIDON altimeter data. Journal of Geophysical Research 30 (17), 1889.

Wyrtki, K., 1961. Physical oceanography of the Southeast Asian water. In NAGA Report Vol. 2, Scientific Result of Marine Investigation of the South China Sea and Gulf of Thailand 1959–1961, Scripps Institution of Oceanography, La Jolla, California, 195pp.

Xu, X.Z., Qiu, Z., Chen, H.C., 1982. The general descriptions of the horizontal circulation in the South China Sea. In: Proceedings of the 1980 Symposium on Hydrometeology

of the Chinese Society of Oceanology and Limnology, Science Press, Beijing (in Chinese with English abstract), pp. 137–145.

Yanagi, T., Takao, T., Morimoto, A., 1997. Co-tidal and co-range charts in the South China Sea derived from satellite altimetry data. Lamer 35, 85–93.

Ye, A.L., Robinson, I.S., 1983. Tidal dynamics in the South China Sea. Geophysical Journal of the Royal Astronomical Society 72, 691–707.

Yu, M., 1984. A preliminary study of tidal characteristics in the South China Sea. Acta Oceanologica Sinica 6, 293–300 (in Chinese).